Geoscientific
Model Development
Discussions

Open Access

OMI NO$_2$ column densities over North American urban cities: the effect of satellite footprint resolution

H. C. Kim[1,2]**, P. Lee**[1]**, L. Judd**[3]**, L. Pan**[1,2]**, and B. Lefer**[3]

[1]NOAA/Air Resources Laboratory, College Park, MD, USA
[2]UMD/Cooperative Institute for Climate and Satellites, College Park, MD, USA
[3]University of Houston, Houston, TX, USA

Correspondence to: H. C. Kim (hyun.kim@noaa.gov)

GMDD

8, 8451–8479, 2015

OMI NO$_2$ column densities over North American urban cities

H. C. Kim et al.

Title Page

Abstract	Introduction
Conclusions	References
Tables	Figures

Back | Close

Full Screen / Esc

Printer-friendly Version

Interactive Discussion

Abstract

Nitrogen dioxide vertical column density (NO_2 VCD) measurements via satellite are compared with a fine-scale regional chemistry transport model, using a new approach that considers varying satellite footprint sizes. Space-borne NO_2 VCD measurement has been used as a proxy for surface nitrogen oxide (NO_x) emission, especially for anthropogenic urban emission, so accurate comparison of satellite and modeled NO_2 VCD is important in determining the future direction of NO_x emission policy. The National Aeronautics and Space Administration Ozone Monitoring Instrument (OMI) NO_2 VCD measurements, retrieved by the Royal Netherlands Meteorological Institute (KNMI), are compared with a 12 km Community Multi-scale Air Quality (CMAQ) simulation from the National Oceanic and Atmospheric Administration. We found that OMI footprint pixel sizes are too coarse to resolve urban NO_2 plumes, resulting in a possible underestimation in the urban core and overestimation outside. In order to quantify this effect of resolution geometry, we have made two estimates. First, we constructed pseudo-OMI data using fine-scale outputs of the model simulation. Assuming the fine-scale model output is a true measurement, we then collected real OMI footprint coverages and performed conservative spatial regridding to generate a set of fake OMI pixels out of fine-scale model outputs. When compared to the original data, the pseudo-OMI data clearly showed smoothed signals over urban locations, resulting in roughly 20–30 % underestimation over major cities. Second, we further conducted conservative downscaling of OMI NO_2 VCD using spatial information from the fine-scale model to adjust the spatial distribution, and also applied Averaging Kernel (AK) information to adjust the vertical structure. Four-way comparisons were conducted between OMI with and without downscaling and CMAQ with and without AK information. Results show that OMI and CMAQ NO_2 VCDs show the best agreement when both downscaling and AK methods are applied, with correlation coefficient $R = 0.89$. This study suggests that satellite footprint sizes might have a considerable effect on the measurement of fine-scale urban NO_2 plumes. The impact of satellite footprint resolution should be

considered when using satellite observations in emission policy making, and the new downscaling approach can provide a reference uncertainty for the use of satellite NO$_2$ measurements over most cities.

1 Introduction

Tropospheric nitrogen dioxide, NO$_2$, is an important component of urban atmospheric chemistry. It is one of the major pollutants affecting humans and the biosphere (Chauhan et al., 2003; Kampa and Castanas, 2008), and works as an important precursor in tropospheric ozone chemistry and aerosol formation. Continuous monitoring of tropospheric NO$_2$ is important to understand urban air quality and changes in anthropogenic emissions. NO$_2$ is also used as an important indicator for traffic and urbanization (Rijnders et al., 2001; Ross et al., 2006; Studinicka et al., 1997).

Tropospheric NO$_2$ has been measured from space since the mid-1990s; the Global Ozone Monitoring Experiment (GOME, 1996–2003, onboard the European Remote Sensing-2), Scanning Imaging Absorption SpectroMeter for Atmospheric CHartographY (SCIAMACHY, 2002–2012, onboard ENVISAT), Ozone Monitoring Instrument (OMI, 2004–present, onboard Aura), and GOME-2 (2007–present, onboard MetOp-A and 2013–present on MetOp-B) have all been used for the detection of NO$_x$ emission from natural and anthropogenic sources (Beirle et al., 2004; Boersma et al., 2007; Kim et al., 2006, 2009; Konovalov et al., 2006; Lamsal et al., 2008; Martin et al., 2003; Napelenok et al., 2008; Richter et al., 2005; van der A et al., 2006, 2008)

NO$_2$ plumes from urban anthropogenic sources, especially from point and mobile sources, usually have a fine structure, as small as a few hundred meters and as large as 10–20 km, as reported in comparisons of column NO$_2$ based on in situ observations and modeled calculations (Heue et al., 2008; Valin et al., 2011; Ryerson et al., 2001). Heue et al. (2008) used an airborne instrument based on imaging Differential Optical Absorption Spectroscopy (iDOAS) to build a two-dimensional distribution model of urban plumes. By comparing NO$_2$ column densities over the industrialized South African

Full Screen / Esc

Printer-friendly Version

Interactive Discussion

Highveld with OMI and SCIAMACHY measurements, they demonstrated that iDOAS shows strong enhancements close to industrial areas, 4–9 times higher than measurements from OMI and SCIAMACHY. Previous studies have demonstrated that modeled ozone production depends strongly on the spatial scale of the modeling grid due to the nonlinear dependence of ozone production on NO$_x$ concentration (e.g., Cohan et al., 2006; Gillani and Pleim, 1996; Liang and Jacobson, 2000; Sillman et al., 1990), so an accurate comparison of urban NO$_2$ plumes in fine scale is crucial for understanding surface ozone chemistry and air pollution over urban cities. Using 1-D and 2-D models, Valin et al. (2011) computed the resolution-dependent bias in the predicted NO$_2$ column, demonstrating large negative biases over large sources and positive biases over small sources at coarse model resolution.

The inhomogeneity of urban NO$_2$ plumes within the scale of satellite footprint pixels is of rising interest as satellite-based measurements are being compared with fine-scale modeling (Beirle et al., 2004, 2011; Hilboll et al., 2013). Richter et al. (2005) showed that there are considerable differences between GOME and SCIAMACHY observations for locations with steep gradients in the tropospheric NO$_2$ columns, while these observations agree very well over large areas of relatively homogeneous NO$_2$ signals. Hilboll et al. (2013) argued that these effects result from spatial smoothing that differs depending on the ground resolution of the instruments, so the inherent spatial heterogeneity of the NO$_x$ fields must be considered when studying them over small, localized areas. Hilboll et al. (2013) also presented approaches to account for instrumental differences while preserving individual instruments' spatial resolutions. In comparing GOME and SCIAMACHY, they used an explicit climatological correction factor to convolve GOME pixels (40 km × 320 km) with better-resolution SCIAMACHY (30 km × 60 km) data, producing a combined data set for studying long-term trends.

In this study, we try to investigate and to quantify the uncertainty resulting from the geometry of OMI satellite-based NO$_2$ VCD measurements by comparing these data to a fine-scale regional quality model. First, a pseudo-OMI data set is built from the outputs of fine-scale model simulations, and then these results are compared to model

data in order to quantify the impact from pure differences in geometry. Second, we extend the basic concept of Hilboll et al. (2013) to apply spatial-distribution information from the fine-scale model to the OMI measurements, and demonstrate how the new approach adjusts the original OMI measurements. Satellite and model data are described in Sect. 2. Construction of pseudo-OMI data and the quantification of the impact of pixel geometry are discussed in Sect. 3. In Sect. 4, the downscaling approach is discussed; Sect. 5 concludes and discusses the implications of findings for emission policy decision-making.

2 Data

OMI: We utilized OMI tropospheric NO_2 VCD data, retrieved by the Royal Netherlands Meteorological Institute (KNMI). The OMI instrument, onboard NASA's Earth Observing System Aura satellite, is a nadir-viewing imaging spectrograph measuring backscattered solar radiation with a measuring wavelength ranging from 270 to 500 nm and with a spectral resolution of about 0.5 nm. Its telescope has a 114° viewing angle, which corresponds to a 2600 km-wide swath on the surface. In its normal global operation mode, its pixel size is 13 km (along) × 24 km (across) at nadir, which can be reduced to 13 km × 12 km in zoom mode (Levelt et al., 2006). Data were downloaded from the European Space Agency's (ESA) Tropospheric Emission Monitoring Internet Service (TEMIS; http://www.temis.nl/airpollution/no2.html). DOMINO version 2.0 retrieval based on the Differential Optical Absorption Spectroscopy (DOAS) technique was used for the study. We disregarded data pixels with cloud fractions over 40 % or other contaminated pixels using quality flags. Details on the NO_2 column retrieval algorithms and error analysis are described in Boersma et al. (2004, 2007).

NAQFC: The US National Air Quality Forecast Capability (NAQFC) provides daily, ground-level ozone predictions using the Weather Forecasting and Research non-hydrostatic mesoscale model (WRF-NMM) and CMAQ framework across the CONUS with a 12 km resolution domain (Chai et al., 2013; Eder et al., 2009). In our analy-

sis, we used the experimental version of NAQFC, which uses WRF-NMM with B-grid (NMMB) as a meteorological driver and the CB05 chemical mechanism. Meteorological data is processed using the PREMAQ, which is a special version of the Meteorology–Chemistry Interface Processor (MCIP) designed for the NAQFC system.

3   Construction of pseudo-OMI data

OMI footprint pixel size increases as the viewing angle deviates from the nadir direction to the edge of swaths. Figure 1 shows the actual size distributions of OMI pixels collected during September 2013. The blue line indicates size distribution counts for each $50\,km^2$ bin, while the red line indicates the cumulative distribution of the OMI pixel sizes. The size distribution has high occurrences near $300\,km^2$, as expected from the OMI's resolution at the nadir (that is, $13 \times 24 = 312$). However, many pixels still have larger sizes; around half of total pixels are larger than $500\,km^2$, and 20 % of total pixels are larger even than $1000\,km^2$. Geographical coverage rapidly increases with pixel size, so deciding a threshold for footprint pixel sizes and available coverage may present a serious dilemma.

Figure 2 shows the relationship between OMI footprint pixel size and actual geographical coverage over the Contiguous United States (CONUS). With 1 July 2011 data, 25 % of OMI pixel sizes are less than $342\,km^2$, and they cover 1.4 % of the CONUS domain. CONUS coverage changes to 11.5, 24.0, and 58.8 % when 50, 75, and 100 % of OMI pixels are used, respectively. Using only finer data may provide detailed information, but they represent only a small part of all the data. If we also use coarser-resolution data, they provide more coverage but tend to be biased over areas with spatial gradient, as discussed in the previously mentioned studies (Hilboll et al., 2013). We therefore estimated the theoretical range of biases deriving from this geometric effect by constructing a pseudo-OMI data set out of a fine-scale model. Using the fine-scale regional CMAQ simulations and assuming this model represents a true

Full Screen / Esc

Printer-friendly Version

Interactive Discussion

world, we constructed a dataset to mimic OMI instrument measurement of this modeled world.

In order to construct the pseudo-OMI data, we utilized a conservative spatial regridding technique to perform a lossless conversion of gridded modeling outputs into actual OMI footprint pixels. Figure 3 demonstrates the concepts of conservative regridding. The gray grid cells are 12 km grid cells for modeling – zoomed on the Houston region as an example – and the blue lines are actual OMI pixel coverage. The blue, shaped pixel is an example of an actual OMI pixel, while the pink boxes are model grid cells overlaid by the example OMI pixel. The numbers in the grid cells are calculations of the fractional area overlaid by the OMI pixel for each cell using the Sutherland–Hodman polygon-clipping algorithms available from the IDL-based Geospatial Data Processor (Kim et al., 2013); 0.74 means the OMI pixel covers 74 % of the corresponding grid cell. The pseudo-OMI value for the blue OMI pixel area in Fig. 3 can be estimated as:

$$P_j = \frac{\sum (p_i \cdot f_{i,j})}{\sum f_{i,j}} \tag{1}$$

where i and j are indices for the model grid cell and OMI pixel, respectively. $f_{i,j}$ indicates the fractional area of cell i overlaid by OMI pixel j.

Figure 4 compares the spatial distributions of CMAQ NO_2 VCD (assumed to be a true world) and pseudo-OMI (pOMI) NO_2 VCD, along with the difference and percentage difference, (pOMI-CMAQ)/CMAQ × 100, over the northeastern United States. It is evident that there are prominent differences between the original fine-scale modeled NO_2 VCD and reconstructed pseudo-OMI distribution, especially over and near urban locations. As expected from the smoothing effects of larger pixel sizes, pOMI shows a slightly smoothed transition from urban cores to suburban, and most of the sharp peaks near small cities are gone in the pOMI distribution. As already mentioned, this is purely a result of geometry. We can see that, for all the major cities, pOMI underestimates the actual NO_2 VCD values while overestimating at the boundaries of major cities, as clearly seen in the New York, Pittsburgh, Philadelphia, Baltimore, and Washington D.C.

areas. This effect is also prominent in locations with small but strong NO_x emission sources, such as power plants or small cities such as Norfolk, VA. It should be noted that these discrepancies result from purely geometric effects deriving from OMI's designed pixel sizes and are around ± 5–10×10^{15} # cm^{-2}, with 20–30 % underestimation or overestimation biases for major cities and more than 100 % under- or overestimation for local cities like Norfolk and Richmond, VA. In the next section, we introduce a new approach – the conservative downscaling method – to reduce this effect of resolution due to varying OMI footprint pixel sizes.

4   OMI NO$_2$ VCD downscaling

As described in the previous section, urban NO_2 plumes usually have too fine of a spatial structure compared to OMI's measuring footprints. In this section, we introduce a new approach for adjusting those geometric effects. Downscaling is a common concept in meteorological simulations, used especially in global circulation models to provide initial and boundary conditions for regional models. We use a similar concept, describing a downscaling method in data processing as a special case of spatial regridding that provides further details through the incorporation of additional information into a set of coarse-resolution data. This approach differs from simply increasing the resolution, as the raw, coarse data are restructured using a set of logics, analogous to a regional meteorological model that downscales global meteorology using its own set of physical and thermal field balances. Conceptually, we use a calculation process reversed from that used to construct the pseudo-OMI data set.

Figure 5 graphically depicts the steps of conservative downscaling from OMI pixels. Figure 5a shows actual OMI NO_2 VCD measurements over Los Angeles on 4 May 2010, and Fig. 5b shows the corresponding CMAQ NO_2 VCD calculated from NAQFC modeling outputs at the same time and location. As readers can easily see, OMI footprint pixels are much bigger (~ 650 km^2) than are CMAQ grid cells ($12 \times 12 = 144$ km^2). As a result, an OMI pixel can overlay more than 10 CMAQ grid

cells, as demonstrated in Fig. 5b (black box representing the OMI pixel). We collected those CMAQ pixel values and then normalized them so that the total value of each grid cell sums to one. We call this a spatial-weighting kernel (Fig. 5c), and we apply this weighting kernel to the original OMI measurement. As a result, we generate

5 a reconstructed OMI pixel with finer structure but without any loss of original quantity. Summing the reconstructed pixels gives the original OMI pixel measurement. It should be noted that we strictly apply this method conservatively; theoretically, if there are no missing or duplicated pixels, the quantity of the original data is numerically preserved. This method can be summarized as fusing a satellite-measured "quantity" with mod-

10 eled "spatial information"; the strength of the modeled NO_2 field does not at all affect the result.

As expected, the accuracy of this method indeed depends on the model's performance, especially regarding its wind-field simulation and inputs of emission source locations. Considering the uncertainties resulting from emission source locations, the air-

15 quality community has had an excellent archive of geographical information about the geophysical locations of emission sources thanks to the efforts of US EPA, although the strengths of these sources are somewhat highly uncertain. As just described, however, the downscaling method is not affected by emission strength, so we do not think that the uncertainty associated with emission is very high. Wind field is important for simu-

20 lating NO_2 plume transport. With the short lifetime of NO_2, especially during summer, the spatial distribution of NO_2 plumes is strongly determined by the location of emission sources. Improving information about emission-source locations would somewhat improve the model, but it is more important to note that the downscaling method tends to convert the error characteristics. Near urban cores, OMI's coarse footprint resolu-

25 tion always causes unidirectional, systematic biases, with underestimation near urban cores and overestimation at the urban boundary. Using the downscaling method, these systematic biases from resolution are converted to random bias from wind-field error. Since these biases are random, they may be corrected by averaging over a certain time period, unlike the systematic bias resulting from resolution.

Title Page

Abstract | Introduction

Conclusions | References

Tables | Figures

◄ | ►

◄ | ►

Back | Close

Full Screen / Esc

Printer-friendly Version

Interactive Discussion

4.1   2010 CalNex campaign case

We applied the downscaling technique to compare OMI and downscaled OMI with aircraft-borne measurements from the California Research at the Nexus of Air Quality and Climate (CalNex) campaign. The CalNex field study was conducted in California from May to July 2010 and focused on atmospheric-pollution and climate-change issues, including an emission inventory, atmospheric transport and dispersion, atmospheric chemical processing, cloud–aerosol interaction, and aerosol radiative effects (Ryerson et al., 2013). Here, we compared NO_2 VCD observations from the campaign's P3 flight with corresponding OMI measurements using both the standard and downscaling methods. More detailed descriptions regarding data preparation and a discussion of the influence of environmental inhomogeneity and urban NO_2 plumes are provided by Judd et al. (2015).

Figure 6 shows scatter-plot comparisons between the P3 measurements and OMI NASA standard product (Fig. 6a), OMI KNMI product (Fig. 6b), and OMI KNMI downscaled (Fig. 6c) for three days: 4, 7, and 16 May 2010. As reported, the OMI NO_2 VCD tends to underestimate near the Los Angeles urban area. The KNMI retrieval showed a slightly better comparison with slope = 0.73 and $R = 0.85$, while the downscaled product clearly showed the best agreement with the P3 measurements, $R = 0.88$ and slope = 1.0. Deviations still remain from a true one-to-one line even with the downscaling method; these are possibly caused by errors in wind field simulation. We expect these random errors to average out as the amount of available data increases. The downscaling method seems to work even with daily time-scale data sets.

Figure 7 compares OMI NO_2 VCD spatial distributions for the original KNMI products with downscaled products for 4 May 2010, the day when the downscaling method gave the most dramatic changes in the spatial distribution. In the original retrieval, OMI pixels were coarse and mostly smoothed out over Los Angeles. However, by applying the downscaling technique, the adjusted OMI data show a shape much closer to the urban boundary and enhanced NO_2 VCD values at the center of Los Angeles, agreeing

very well with the P3 aircraft measurements. On 7 May (not shown), the downscaling method reproduced several peak values very well but failed to generate a clean spot at the edge of Los Angeles. For 16 May (not shown), the changes from downscaling are not dramatic due to generally low NO_2 concentrations, but the downscaling method still showed slight enhancement.

4.2 Comparison with NAQFC

Comparing modeled NO_2 VCD to satellite-observed NO_2 VCD has been a popular way to evaluate the NO_x emission inventory. Since modeled NO_2 VCD and satellite NO_2 VCD have different optical and vertical properties, some researchers have used additional processing to fairly compare satellite and modeled column densities. In this section, we performed vertical and spatial adjustment by applying Averaging Kernel (AK) information in conjunction with the downscaling technique. First, we compared NAQFC NO_2 VCD with and without AK to OMI NO_2 VCD with and without downscaling processing.

The sensitivity of the instrument to tropospheric tracer density is highly height-dependent. Since the measured tracer profile may have large systematic errors as a result, the retrieved tracer columns should be interpreted with proper additional information (Eskes and Boersma, 2003). An AK stores an instrument's relative sensitivity to the abundance of the target species for each layer throughout the atmospheric column (Bucsela et al., 2008) and can be applied to a modeled atmospheric column for a fair comparison with satellite retrievals. For each OMI DOMINO product pixel, 34 layers of AKs are provided. We first converted total AK to tropospheric AK, AK_{trop}, by applying the total air mass factor (AMF) and tropospheric AMF, and we then applied AK_{trop} to model layers before vertically integrating, as described by Herron-Thorpe et al. (2010). When multiple OMI pixels overlaid a model grid cell, we conducted the conservative spatial remapping method explained above.

Figure 8 compares the monthly averaged NO_2 VCD distributions for CMAQ without and with AK (Fig. 8a and b, respectively) and for OMI NO_2 VCD without and with

downscaling (Fig. 8c and d, respectively). In general, AK-applied CMAQ NO_2 VCD tends to be slightly lower than CMAQ NO_2 VCD without AK information. On the other hand, while OMI NO_2 VCD without DS shows a much smoother pattern, the DS-applied OMI reconstructs the sharp spatial structures near urban areas. DS-applied OMI NO_2
5   VCD is evidently able to construct sharp gradients near cities, and especially near middle-size cities.

Figure 9 compares CMAQ and OMI NO_2 VCDs using AK and DS methods together. Figure 9a shows a scatter-plot comparison between CMAQ and OMI NO_2 VCDs at US Environmental Protection Agency Air Quality System (AQS) surface-monitoring site
10   locations. In this comparison, CMAQ NO_2 VCDs are much higher compared to OMI NO_2 VCDs, implying that the CMAQ simulation possibly overestimates NO_x emissions. Figure 9c compares OMI and CMAQ NO_2 VCD with AK information applied; estimated CMAQ NO_2 VCD is reduced, showing better agreement with OMI NO_2 VCD. Readers may notice that high CMAQ pixels are shifted to the left. On the other hand, applying the
15   DS method to OMI shifts OMI pixels vertically (Fig. 9b). Finally, in Fig. 9d, both AK and DS methods are applied; this comparison shows the best agreement between OMI and CMAQ NO_2 VCD pixels. Its correlation coefficient $R = 0.89$ and the slope of line fit is 0.59. Clearly, the application of the AK and DS methods not only improved the satellite-model comparison in the high NO_2 concentration range but also significantly improved
20   the comparison in the low NO_2 range (i.e., 0–10×10^{15} molecules cm^{-2}), implying that this method can help interpret NO_x emission in major and mid-size cities.

The differences in spatial distributions between monthly averaged OMI and CMAQ NO_2 VCDs during September 2013 are shown in Fig. 10. Positive values indicate that CMAQ NO_2 VCD is higher than OMI VCD, which should likely be interpreted as an
25   overestimation of the NO_x emission inventory used in the CMAQ modeling. The difference between the original OMI and CMAQ NO_2 VCDs show strong positive values over most urban locations (Fig. 10a). Applying AK (Fig. 10b) and DS (Fig. 10c) reduce positive biases for major and middle-to-small cities, showing the best agreement when both AK and DS are included. NO_2 VCD is still overestimated over major cities – New

York, Philadelphia, Detroit, and Chicago – as is expected from the continuous trend of NO_x emission reduction, but they are much weaker than in the original comparison. Slight overestimations over Baltimore, Washington D.C., Richmond, and Norfolk have almost disappeared. We also notice considerable underestimation of NO_2 VCD

5　over Pennsylvania and West Virginia, which seems to be an impact of recent shale-gas development (e.g., the Marcellus Shale Play) (Chang et al., 2015) that has not been included in the current NAQFC emission-source inventory. Another interesting feature is that there are spots of underestimation over small cities or local power plants; we therefore suspect the DS method slightly overweights urban emissions due to the lack

10　of soil NO_x emissions in the current modeling system.

5   Conclusions

This study reports that satellite footprint sizes might cause a considerable effect on the measurement of fine-scale urban NO_2 plumes. Comparing OMI NO_2 VCDs over North American urban cities to a 12 km CMAQ simulation from NOAA NAQFC, we

15　found that OMI footprint-pixel sizes are too coarse to resolve urban plumes, resulting in possible underestimation (and overestimation of model NO_2 VCD) over the urban core and overestimation outside. In order to quantify this effect of resolution, we first conducted a perfect-model experiment. Pseudo-OMI data were constructed using fine-scale outputs of a model simulation, assuming that the fine-scale model output is a true

20　measurement. To match the footprint coverage from real OMI pathways, we conducted conservative spatial regridding with the corresponding fine-scale model outputs to generate a set of pseudo OMI pixels.

　　When compared to the original data, the pseudo-OMI data clearly showed smoothed signals over urban locations, with 20–30 % underestimation over major cities and up

25　to 100 % bias over smaller urban areas. We then introduced conservative downscaling of OMI NO_2 VCD using spatial information from the fine-scale model to adjust the spatial distribution, also applying Averaging Kernel (AK) information to adjust the ver-

tical structure. Four-way comparisons were conducted between OMI with and without downscaling and CMAQ with and without AK information. Results show that OMI and CMAQ NO$_2$ VCDs show the best agreement when both downscaling and AK methods are applied, with correlation coefficient R = 0.89.

These results should be considered when using satellite data in the evaluation of emission inventories and translating these data into decision-making around emission policy. Table 1 shows a summary of the comparisons between OMI and CMAQ NO$_2$ VCDs described in Figs. 8 and 9. When CMAQ without AK and OMI with DS are compared, the percentage difference is $(6.43 - 3.61)/3.61 \times 100 = 78\,\%$, implying that the current emission inventory likely overestimates NO$_2$ VCD. Comparing between OMI with DS and CMAQ without AK or between OMI without DS and CMAQ with AK still implies that the current emission inventory is possibly overestimating. However, when both vertical and spatial profiles are adjusted using the AK and DS methods, a slight underestimation is found, $-7\,\%$, in modeled NO$_2$ VCD over AQS monitoring locations, implying that the current inventory possibly underestimates emissions. This may represent an important implication for how spatial information should be considered when investigating fine-scale phenomena such as urban NO$_2$ plumes.

Without question, satellite observations are very useful with their large coverage supplementing sparse surface-monitoring sites. Interpretation of satellite-based measurement, however, should be performed cautiously with consideration of the instrument's characteristics, especially when translating results into policy-making. We expect our current study to provide a reference for the uncertainty of satellite-based information regarding local or regional pollutants, especially until we have the measurement data at more enhanced resolution that will be provided by future satellites, such as TEMPO, TROPOMI, and GEMS.

References

Beirle, S., Platt, U., Wenig, M., and Wagner, T.: Highly resolved global distribution of tropospheric NO_2 using GOME narrow swath mode data, Atmos. Chem. Phys., 4, 1913–1924, doi:10.5194/acp-4-1913-2004, 2004.

Beirle, Steffen, Boersma, K. F., Platt, U., Lawrence, M. G., and Wagner, T.: Megacity emissions and lifetimes of nitrogen oxides probed from space, Science, 333, 1737–1739, doi:10.1126/science.1207824, 2011.

Boersma, K. F., Eskes, H. J., and Brinksma, E. J.: Error analysis for tropospheric NO_2 retrieval from space, J. Geophys. Res., 109, D04311, doi:10.1029/2003JD003962, 2004.

Boersma, K. F., Eskes, H. J., Veefkind, J. P., Brinksma, E. J., van der A, R. J., Sneep, M., van den Oord, G. H. J., Levelt, P. F., Stammes, P., Gleason, J. F., and Bucsela, E. J.: Near-real time retrieval of tropospheric NO_2 from OMI, Atmos. Chem. Phys., 7, 2103–2118, doi:10.5194/acp-7-2103-2007, 2007.

Bucsela, E. J., Perring, A. E., Cohen, R. C., Boersma, K. F., Celarier, E. A., Gleason, J. F., and Veefkind, J. P.: Comparison of tropospheric NO_2 from in situ aircraft measurements with near-real-time and standard product data from OMI, J. Geophys. Res., 113, D16S31, doi:10.1029/2007JD008838, 2008.

Chai, T., Kim, H.-C., Lee, P., Tong, D., Pan, L., Tang, Y., Huang, J., McQueen, J., Tsidulko, M., and Stajner, I.: Evaluation of the United States National Air Quality Forecast Capability experimental real-time predictions in 2010 using Air Quality System ozone and NO_2 measurements, Geosci. Model Dev., 6, 1831–1850, doi:10.5194/gmd-6-1831-2013, 2013.

Chauhan, A., Inskip, H. M., Linaker, C. H., Smith, S., Schreiber, J., Johnston, S. L., and Holgate, S. T.: Personal exposure to nitrogen dioxide (NO_2) and the severity of virus-induced asthma in children, Lancet, 361, 1939–1944, doi:10.1016/S0140-6736(03)13582-9, 2003.

Cohan, D. S., Hu, Y., and Russell, A. G.: Dependence of ozone sensitivity analysis on grid resolution, Atmos. Environ., 40, 126–135, 2006.

Eder, B., Kang, D., Mathur, R., Pleim, J., Yu, S., Otte, T., and Pouliot, G.: A performance evaluation of the National Air Quality Forecast Capability for the summer of 2007, Atmos. Environ., 43, 2312–2320, doi:10.1016/j.atmosenv.2009.01.033, 2009.

Eskes, H. J. and Boersma, K. F.: Averaging kernels for DOAS total-column satellite retrievals, Atmos. Chem. Phys., 3, 1285–1291, doi:10.5194/acp-3-1285-2003, 2003.

OMI NO2 column densities over North American urban cities

H. C. Kim et al.

Title Page

Abstract | Introduction

Conclusions | References

Tables | Figures

◄ | ►

◄ | ►

Back | Close

Full Screen / Esc

Printer-friendly Version

Interactive Discussion

Gillani, N. V. and Pleim, J. E.: Sub-grid-scale features of anthropogenic emissions of NO_x and VOC in the context of regional eulerian models, Atmos. Environ., 30, 2043–2059, doi:10.1016/1352-2310(95)00201-4, 1996.

Herron-Thorpe, F. L., Lamb, B. K., Mount, G. H., and Vaughan, J. K.: Evaluation of a regional air quality forecast model for tropospheric NO_2 columns using the OMI/Aura satellite tropospheric NO_2 product, Atmos. Chem. Phys., 10, 8839–8854, doi:10.5194/acp-10-8839-2010, 2010.

Heue, K.-P., Wagner, T., Broccardo, S. P., Walter, D., Piketh, S. J., Ross, K. E., Beirle, S., and Platt, U.: Direct observation of two dimensional trace gas distributions with an airborne Imaging DOAS instrument, Atmos. Chem. Phys., 8, 6707–6717, doi:10.5194/acp-8-6707-2008, 2008.

Hilboll, A., Richter, A., and Burrows, J. P.: Long-term changes of tropospheric NO_2 over megacities derived from multiple satellite instruments, Atmos. Chem. Phys., 13, 4145–4169, doi:10.5194/acp-13-4145-2013, 2013.

Judd, L., Lefer, B., and Kim, H. C.: Influences of environmental heterogeneity on OMI NO2 measurements and improvements using downscaling, in preparation, 2015.

Kampa, M. and Castanas, E.: Human health effects of air pollution, Environ. Pollut., 151, 362–367, doi:10.1016/j.envpol.2007.06.012, 2008.

Kim, H., Ngan, F., Lee, P., and Tong, D.: Development of IDL-based geospatial data processing framework for meteorology and air quality modeling, available at: http://aqrp.ceer.utexas.edu/projectinfoFY12_13%5C12-TN2%5C12-TN2FinalReport.pdf (Last access: 29 September 2015), 2013.

Kim, S.-W., Heckel, A., McKeen, S. A., Frost, G. J., Hsie, E.-Y., Trainer, M. K., and Grell, G. A.: Satellite-observed US power plant NO_x emission reductions and their impact on air quality, Geophys. Res. Lett., 33, 27749, doi:10.1029/2006GL027749, 2006.

Kim, S.-W., Heckel, A., Frost, G. J., Richter, A., Gleason, J., Burrows, J. P., and Trainer, M.: NO_2 columns in the western United States observed from space and simulated by a regional chemistry model and their implications for NO_x emissions, J. Geophys. Res., 114, D11301, doi:10.1029/2008JD011343, 2009.

Konovalov, I. B., Beekmann, M., Richter, A., and Burrows, J. P.: Inverse modelling of the spatial distribution of NO_x emissions on a continental scale using satellite data, Atmos. Chem. Phys., 6, 1747–1770, doi:10.5194/acp-6-1747-2006, 2006.

Title Page

Abstract | Introduction

Conclusions | References

Tables | Figures

|◄ | ►|

◄ | ►

Back | Close

Full Screen / Esc

Printer-friendly Version

Interactive Discussion

Lamsal, L. N., Martin, R. V., van Donkelaar, A., Steinbacher, M., Celarier, E. A., Bucsela, E., and Pinto, J. P.: Ground-level nitrogen dioxide concentrations inferred from the satellite-borne Ozone Monitoring Instrument, J. Geophys. Res., 113, 16308, doi:10.1029/2007JD009235, 2008.

Levelt, P., van den Oord, G. H. J., Dobber, M. R., Malkki, A., Stammes, P., Lundell, J. O. V., and Saari, H.: The ozone monitoring instrument, IEEE T. Geosci. Remote, 44, 1093–1101, doi:10.1109/TGRS.2006.872333, 2006.

Liang, J. and Jacobson, M. Z.: Effects of subgrid segregation on ozone production efficiency in a chemical model, Atmos. Environ., 34, 2975–2982, doi:10.1016/S1352-2310(99)00520-8, 2000.

Martin, R. V.: Global inventory of nitrogen oxide emissions constrained by space-based observations of NO_2 columns, J. Geophys. Res., 108, 4537, doi:10.1029/2003JD003453, 2003.

Napelenok, S. L., Pinder, R. W., Gilliland, A. B., and Martin, R. V.: A method for evaluating spatially-resolved NO_x emissions using Kalman filter inversion, direct sensitivities, and space-based NO_2 observations, Atmos. Chem. Phys., 8, 5603–5614, doi:10.5194/acp-8-5603-2008, 2008.

Richter, A., Burrows, J. P., Nüss, H., Granier, C., and Niemeier, U.: Increase in tropospheric nitrogen dioxide over China observed from space, Nature, 437, 129–132, doi:10.1038/nature04092, 2005.

Rijnders, E., Janssen, N. A. H., van Vliet, P. H. N., and Brunekreef, B.: Personal and outdoor nitrogen dioxide concentrations in relation to degree of urbanization and traffic density, Environ. Health Persp., 109, 411–417, doi:10.2307/3434789, 2001.

Ross, Z., English, P. B., Scalf, R., Gunier, R., Smorodinsky, S., Wall, S., and Jerrett, M.: Nitrogen dioxide prediction in Southern California using land use regression modeling: potential for environmental health analyses, J. Expo. Sci. Env. Epid., 16, 106–114, doi:10.1038/sj.jea.7500442, 2006.

Ryerson, T. B., Andrews, A. E., Angevine, W. M., Bates, T. S., Brock, C. A., Cairns, B., and Wofsy, S. C.: The 2010 California Research at the Nexus of Air Quality and Climate Change (CalNex) field study, J. Geophys. Res.-Atmos., 118, 5830–5866, doi:10.1002/jgrd.50331, 2013.

Sillman, S., Logan, J. A., and Wofsy, S. C.: The sensitivity of ozone to nitrogen oxides and hydrocarbons in regional ozone episodes, J. Geophys. Res., 95, 1837–1851, doi:10.1029/JD095iD02p01837, 1990.

Title Page

Abstract | Introduction

Conclusions | References

Tables | Figures

◄ | ►

◄ | ►

Back | Close

Full Screen / Esc

Printer-friendly Version

Interactive Discussion

Studinicka, M., Hackl, E., Pischinger, J., Fangmeyer, C., Haschke, N., Köhr, J., and Frischer, T.: Traffic-related NO_2 and the prevalence of asthma and respiratory symptoms in seven year olds, Eur. Respir. J., 10, 2275–2278, doi:10.1183/09031936.97.10102275, 1997.

Valin, L. C., Russell, A. R., Hudman, R. C., and Cohen, R. C.: Effects of model resolution on the interpretation of satellite NO_2 observations, Atmos. Chem. Phys., 11, 11647–11655, doi:10.5194/acp-11-11647-2011, 2011.

Van der A, R. J., Peters, D. H. M. U., Eskes, H., Boersma, K. F., Van Roozendael, M., De Smedt, I., and Kelder, H. M.: Detection of the trend and seasonal variation in tropospheric NO_2 over China, J. Geophys. Res., 111, D12317, doi:10.1029/2005JD006594, 2006.

Van der A, R. J., Eskes, H. J., Boersma, K. F., van Noije, T. P. C., Van Roozendael, M., De Smedt, I., and Meijer, E. W.: Trends, seasonal variability and dominant NO_x source derived from a ten year record of NO_2 measured from space, J. Geophys. Res., 113, D04302, doi:10.1029/2007JD009021, 2008.

OMI NO_2 column densities over North American urban cities

H. C. Kim et al.

Table 1. Comparison of OMI and CMAQ NO$_2$ VCD monthly averages (September 2013) at AQS sites.

	OMI/xDS (mean = 3.61)	OMI/DS (mean = 5.00)
CMAQ/xAK (mean = 6.43)	S = 0.28 R = 0.79 $(6.43 - 3.61)/3.61 \times 100 = 78.1\%$	S = 0.45 R = 0.87 $(6.43 - 5)/5 \times 100 = 28.6\%$
CMAQ/AK (mean = 4.65)	S = 0.39 R = 0.87 $(4.65 - 3.61)/3.61 \times 100 = 28.8\%$	S = 0.59 R = 0.89 $(4.65 - 5)/5 \times 100 = -7.0\%$

Full Screen / Esc

Printer-friendly Version

Interactive Discussion
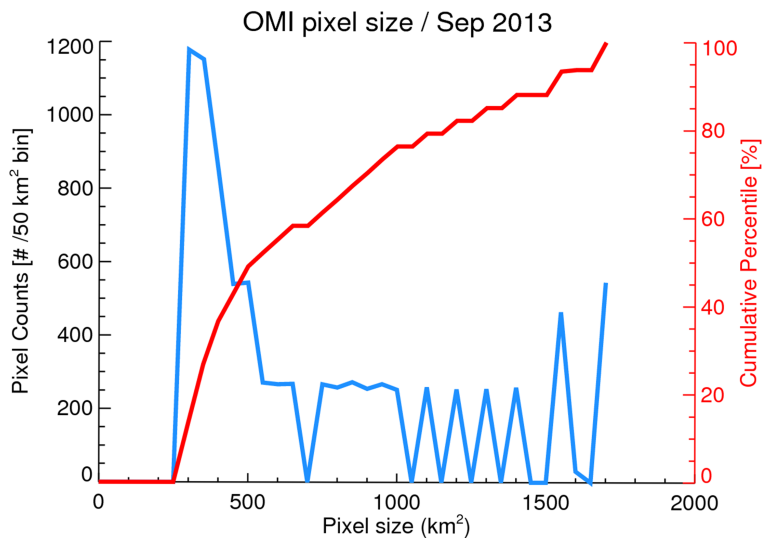
Figure 1. Size distribution of OMI pixel footprint (blue) and its cumulative percentile (red).

(A) Size < 342 km², Pixel=25%,Coverage= 1.4 %

(B) Size < 450 km², Pixel=50%,Coverage= 11.5 %

(C) Size < 721km², Pixel=75%,Coverage= 24.0 %

(D) Size < 1732 km², Pixel=100%,Coverage= 58.8 %
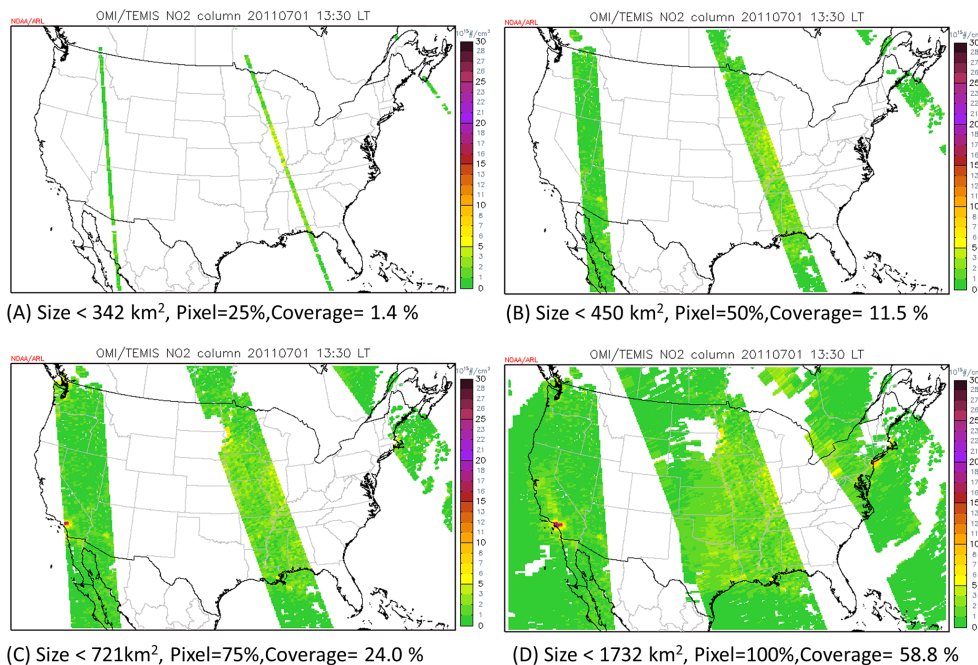
Figure 2. Comparison of OMI footprint-pixel size and actual coverage using **(a)** 25 %, **(b)** 50 %, **(c)** 75 %, and **(d)** 100 % of available pixels.

Title Page

Abstract | Introduction

Conclusions | References

Tables | Figures

⏮ | ⏭

◀ | ▶

Back | Close

Full Screen / Esc

Printer-friendly Version

Interactive Discussion
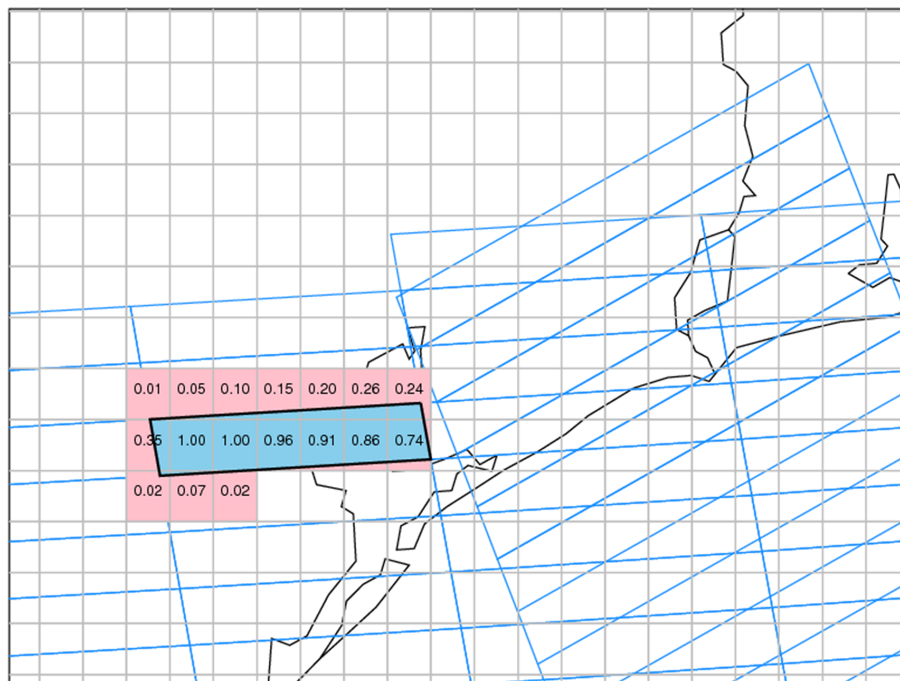
Figure 3. Calculation of pseudo-OMI (pOMI) data. Blue boxes are actual OMI pixel footprints and the gray cells are 12 km grid cells. Fraction of cells overlapped by an OMI pixel are shown, and pOMI (sky blue) data are estimated by a weighted average of the corresponding grid cells (pink).

Title Page

Abstract | Introduction

Conclusions | References

Tables | Figures

|◄ | ►|

◄ | ►

Back | Close

Full Screen / Esc

Printer-friendly Version

Interactive Discussion

Figure 4. Monthly mean distribution of **(a)** CMAQ, **(b)** pOMI NO_2, **(c)** difference (pOMI – CMAQ), and **(d)** percentage difference (pOMI – CMAQ)/CMAQ × 100.
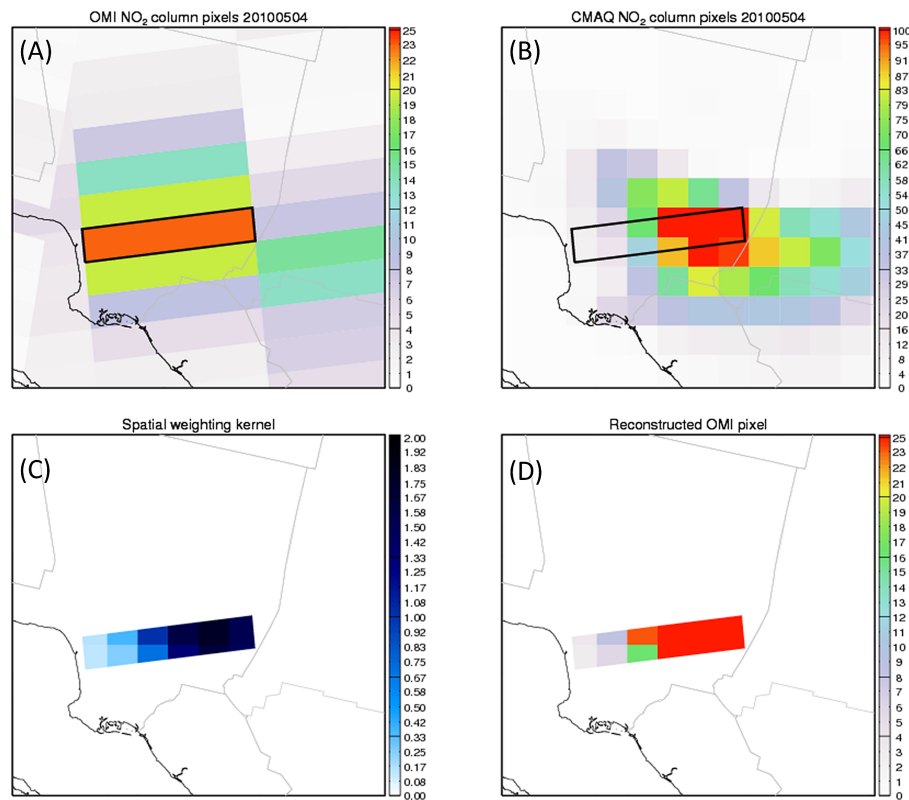
Figure 5. Example of downscaling method. **(a)** Original OMI NO$_2$ VCD, **(b)** 12 km CMAQ NO$_2$ VCD, **(c)** spatial weighting kernel, and **(d)** adjusted OMI NO$_2$ VCD using spatial weighting kernel.

Figure 6. Scatter plots of P3 and OMI NO$_2$ VCD for **(a)** OMI standard products, **(b)** OMI KNMI, and **(c)** OMI KNMI with downscaling.
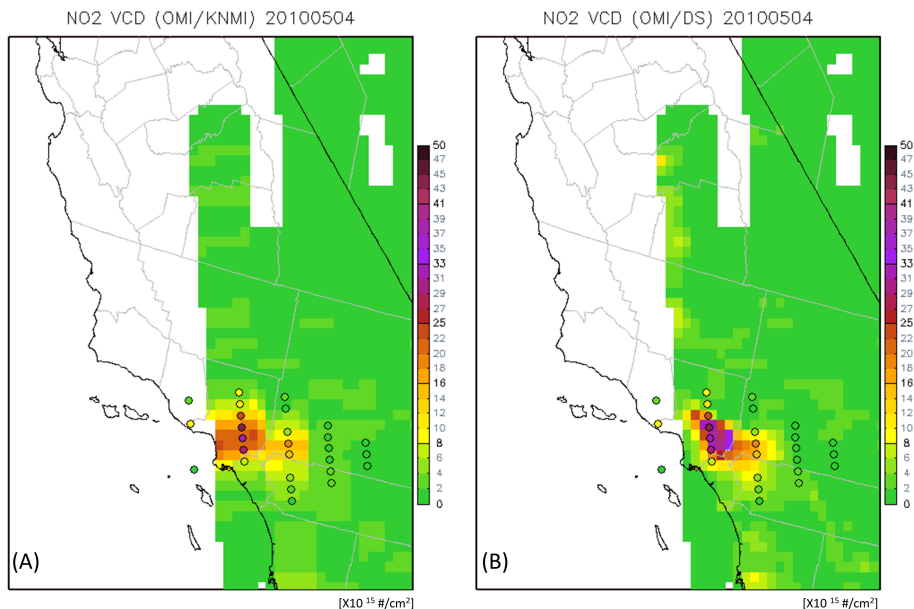
Figure 7. Spatial distribution of P3 NO$_2$ VCDs (circles) and OMI NO$_2$ VCDs for original KNMI product **(a)**, and downscaled OMI **(b)** for 4 May 2010.

Full Screen / Esc

CMAQ NO$_2$ VCD / Sep 2013 / xAK

(A)

CMAQ NO$_2$ VCD / Sep 2013 / AK

(B)

OMI NO$_2$ VCD / Sep 2013 / xDS

(C)

OMI NO$_2$ VCD / Sep 2013 / DS

(D)
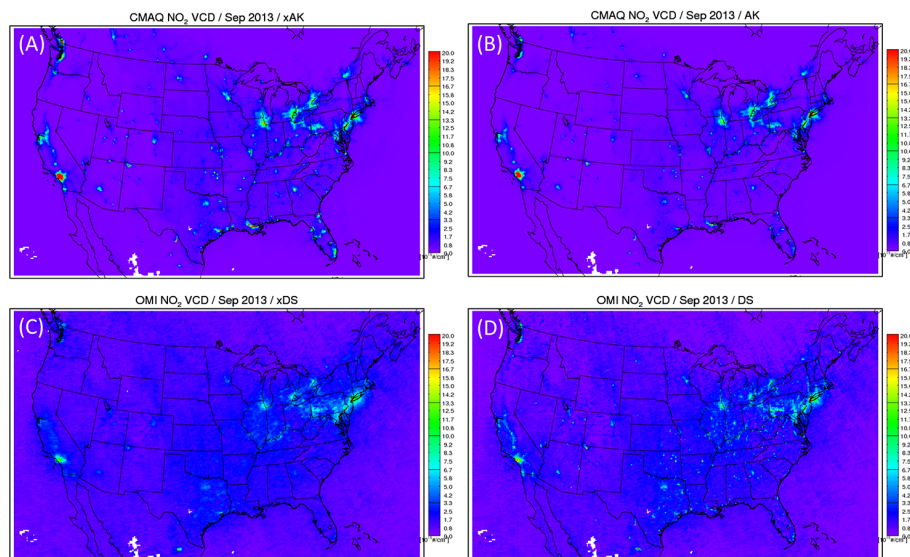
Figure 8. Spatial distributions of **(a)** CMAQ NO$_2$ VCD without AK and **(b)** with AK; **(c)** OMI NO$_2$ VCD without downscaling and **(d)** with downscaling.
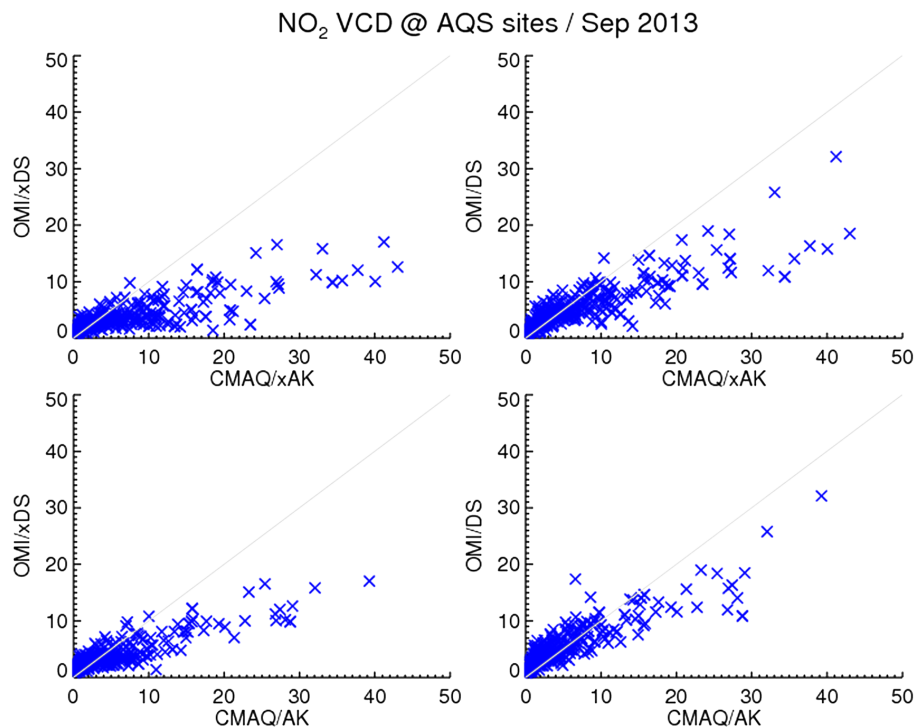
Figure 9. Comparison of OMI and CMAQ NO$_2$ VCD for **(a)** OMI and CMAQ with AK, **(b)** down-scaled OMI and CMAQ with AK, **(c)** OMI and CMAQ with AK, and **(d)** downscaled OMI and CMAQ with AK.
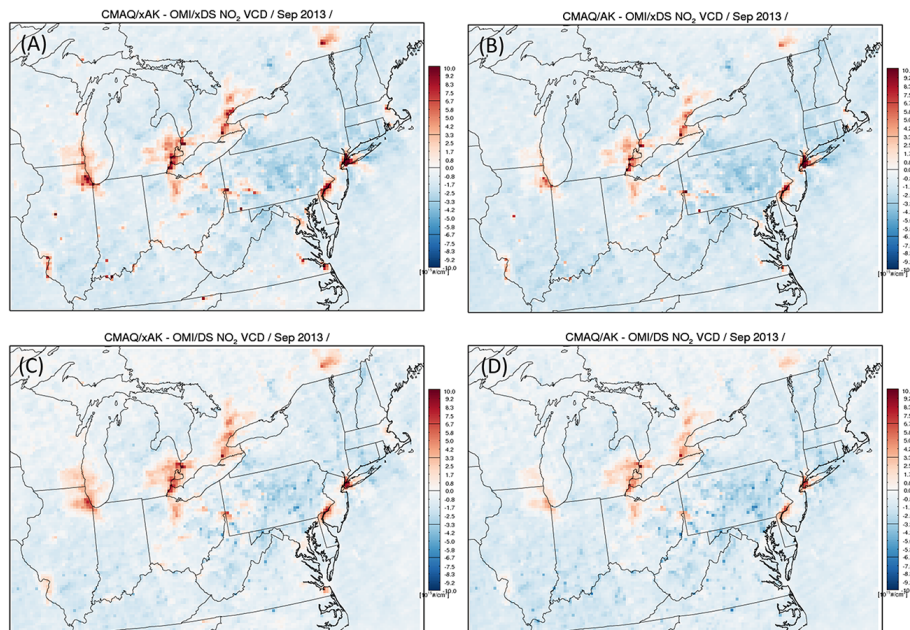
Figure 10. Comparisons of OMI and CMAQ NO$_2$ VCD spatial distributions in the northeast US region.